JOURNAL OF INTERNATIONAL ACADEMIC RESEARCH FOR MULTIDISCIPLINARY
Impact Factor 1.625, ISSN: 2320-5083, Volume 3, Issue 4, May 2015

NOVEL SURFACTANTS SUPPORTED ROOM TEMPERATURE SYNTHESIS OF NANOSIZED NICKEL OXIDE: γ RADIOLYSIS

Dr. K NAVINKIRAN*
Dr. ANJALI A ATHAWALE**

*Former Research Scholar, Dept. of Chemistry, Savitribhai Phule Pune University, Pune , India
**Research Guide, Dept. of Chemistry, Savitribhai Phule Pune University, Pune, India

ABSTRACT

A novel solution based synthesis of nanosized nickel oxide is being carried out using steady state high energy γ radiolysis. Synthesis of nickel oxide was carried out by varying the volume ratios of surface directing agents like cetrimide (CTAB) and tetra ethyl ammonium bromide (TEAB). Concentrations of the surfactants were optimized along with the change in volume ratio of iso-propanol and water was varied from 100% to 20%. The progress of the reactions was found out by using UV-visible spectroscopy. The peak at ~ 410 cm^{-1} as observed in the FT-IR spectroscopy indicates the formation of the oxide. The major peaks as noted in the X-ray diffractograms corresponds to the formation of Ni_2O_3 as the major phase. Spherical or partially spherical shaped particles are seen in the transmission electron microscope. HRTEM establishes the morphology along with the Ni_2O_3 as the major product formed during the synthesis. X-ray photoelectron spectroscopy confirms the oxidation state as Ni^{3+} with the maximum intensity peak observed at ~ 855.80 eV.

KEYWORDS: γ-Radiolysis; Spherical Shaped Particles; X-Ray Diffraction; X-Ray Photoelectron Spectroscopy.

INTRODUCTION

The synthesis of nanoparticles has been extensively investigated in the past few decades [1]. Although the size of nanoparticles cannot be exactly controlled even in physical techniques, it is possible to narrow the size distribution by controlling the parameters like evaporation rate and system pressure [2]. Due to limitation of physical vapour deposition technique, majority of the work in the area of nanoparticles production have involved chemical routes where narrow and controlled size distribution of nanoparticles is obtained. In a simple technique, chemical reduction of metal salt dissolved in appropriate solvent can lead to the formation of nanoparticles with varying size and shape distribution [3]. Several techniques such as sol–gel [4], spray pyrolysis [5], thermal decomposition [6-8] and hydrothermal / solvothermal synthesis [9,10] have been proposed for producing metal oxide

nanoparticles. However, these methods require long reaction times and use of organic solvents, which made additional processes necessary for the complete synthesis process. Some of the existing methods of synthesis suffer from the drawbacks that are mainly related to the production of the particles in a controllable manner in terms of particle size, mono-dispersity, and shape. Use of organic solvents which may lead to some environment issues like hazards and some degradation may be an issue. Alternative methods for the production of nanoparticles are desired due to rapid advances in nanotechnology and its applications in almost every aspect of civilian and military technologies [11].

Nano structured oxides prepared in the form of rods, fibres, ribbons, channels and other shapes display unique properties that make them suitable for many new applications [12]. However, particles formed in this manner tend to agglomerate, making it necessary to use appropriate surfactants [13]. Because of quantum and other size effects, the properties of nanosized oxide materials differ from those of the bulk. Nickel oxides are used for various applications such as catalyst [14], battery cathode [15,16], gas sensors [17], electrochromic films [18,19] and magnetic material [20,21].

Authors here report the synthesis of nickel oxide nano particles using steady state γ-radiolysis technique. Aqueous salt solutions of nickel were used and reduced in the presence of aniline which acts as a stabilizer and capping agent such as CTAB and TEAB. IPA-water combinations were used as reducing agents. The corresponding progress of reactions and the possible functional groups present in the materials were found out by UV-visible and Fourier transform infra red spectroscopy respectively. X-ray diffraction (XRD), transmission electron microscopy (TEM), high resolution transmission electron microscope (HRTEM) and X-ray photoelectron spectroscopy (XPS) were used for evaluating for the size and its distribution, composition and the phase purity of the synthesized material.

Experimental methods of synthesis and characterizations

Materials used

All the chemicals used in the experimental work carried out were of A.R. grade with more than 98% purity. Precursor salt such as nickel nitrate [$Ni(NO_3)_2,6H_2O$] was procured from Loba Chime, India. This was kept in air tight glass bottles with ground glass joints and then stored in desiccator. Aniline [$C_6H_5NH_2$] as stabilizer, iso-propanol [$(CH_3)_2CHOH$] as reducing agent, and ammonium persulphate [$(NH_4)_2S_2O_8$] and surfactants such as CTAB used for the synthesis were from Qualigens, India and TEAB from CDH, India, respectively.

Aniline was distilled and stored under dark in refrigeration prior to use. All the other reagents were used as received without further purification. 0.1 M stock solution of nickel salt was prepared by using high purity Milli Q water having resistivity of 18 MΩcm^{-1}. 0.01M concentration of surfactant solutions were freshly prepared in IPA and used in the synthesis.

1) Preparation of nanosols and composites

Experiments were conducted with CTAB and TEAB as surfactants which also played the role of capping agents. Ratio of concentration of these surfactants with metal ions was varied from 0.25:1.0 to 1.0:1.0. Optimised concentrations of these surfactants correspond to 1.0 x 10^{-3} M [1.0:1.0] for nickel oxide nanosols. Further studies were carried out with and without surfactants at volume ratios of IPA to water from 100% to 20% were added in appropriate volume ratio. The reaction mixture was subjected to ^{60}Co gamma irradiation source with a dose rate of 5.1 Gy**.**min^{-1} at room temperature. The composites of these sols were prepared by drop wise addition of ammonium persulphate (oxidizing agent) from a soxhlet funnel under constant uniform stirring at 5^{o}C for 2 hours. Synthesized nanocomposites were obtained by keeping these materials on a permanent magnet, then washing with respective solvents followed by filtration and drying these powders in an oven at 50^{o}C for 24 hours.

Characterisation techniques involved

1) UV-visible analysis

Absorption spectra of all the samples were recorded on a Shimadzu (1650 PC) taking the solutions in a 5 cm quartz cuvette. Spectra were taken at regular intervals with reference to a blank solution without metal ion under identical conditions using double beam spectrophotometer having a path length of 1.00 cm, operated at a resolution of 1 nm from wavelength 200 nm to 1100 nm.

2) Fourier Transform Infrared Spectroscopy

FT-IR spectroscopy measurements were carried out using a Shimadzu 8400 spectrophotometer at a range (4000 – 350 cm^{-1}). For this, 10 mg of the dried composite sample was mixed with 100 mg of spectroscopic grade potassium bromide (KBr), and the resultant suspension was mixed uniformly by using a mortar and pestle. A small portion of the sample was pressed into a transparent homogeneous pellet at approximately 20 kpsi. Typically 30 scans per spectrum were recorded at 4cm^{-1} resolution in the transmittance mode. The background spectrum was automatically subtracted.

3) X- ray diffractograms

Phase identification for finding out the level of purity in samples and structural analysis were performed by rotating anode X-ray powder diffraction For XRD studies, the samples were directly placed onto the sample holder. Powder patterns were recorded with a PA Nalytical X pert Pro. Samples were placed in glass sample holders CuK_{α} radiation was the light source using nickel filter with applied voltage of 40 kV and a current of 30 mA. The inter planar distances 'd' were calculated according to Bragg's law and then compared to the ASTM standards for finding out the crystal structure. The glancing angle varied from 10^{o} to 80^{o}.

4) Transmission electron microscopy

Technai G20 twin microscope joined with Gatan imaging filter along with a Philips CM 200 microscope fitted with CCD camera operating at an accelerating voltage of 200 kV was employed for the microscopic analysis of the samples. These samples were sonicated with mother liquor (solvent used for preparing nano sols) for 1 min followed by pipetting out 2 µl sol on carbon coated copper grid and subsequently putting them on filter paper to remove excessive solution from the grid. Excess solvent was evaporated in air. Point to point resolution of the equipment was 0.23 nm.

Electron diffraction patterns were obtained at a camera length of 300 mm using an aperture of the beam having diameter 10 µm. The particle size and inter planar distance 'd' was analyzed by Gatan Imaging System. EDAX system joined with TEM is manufactured by EDAX Corporation USA.

5) High resolution transmission electron microscopy

HRTEM was carried out utilizing Technai G20-twin microscope. The lattice fringes of the material were found at an accelerating voltage of 200 kV with point to point resolution as 0.144 nm. The lens type used is super twin lenses. A CCD camera along with Gatan imaging filter is attached to HRTEM. Specimens were prepared by injecting the droplets of diluted solution deposited on a copper grid covered by a thin carbon film followed by evaporation in air. Fringe widths were calculated by using the Gatan imaging software

6) X-ray photoelectron spectroscopy

XPS measurements were carried out on a Perkin Elmer Spectrometer equipped with a hemispherical analyzer. XPS spectra were acquired using MgK_{α} (1253.6 eV) source, operating at a voltage of 12–14 kV and current of 10–20 mA. Samples were mounted onto a

conductive adhesive Cu tape. Spectra were obtained at room temperature and at an operating vacuum ~ 1 x 10^{-8} Torr in the analysis chamber. Calibration was performed using standard method i.e. Au 4f7/2 line for external (spectrometer calibration) and carbon 1s as a line internal correction. The core level spectra were corrected for background using the Shirley algorithm and the chemically distinct species were resolved using a nonlinear least square procedure.

Results and Discussion

1) UV-visible spectroscopy

The advancement of the reaction, intermediate and the final product formation were studied by using the UV-visible spectroscopy. The reaction rates were monitored by dissolving 0.1 M aniline, 1.0 x 10^{-3} M Ni^{2+} ions, with and without surfactants in IPA. Solutions containing equivalent amount of aniline, surfactant and the solvent except the metal ions were irradiated under identical conditions and were used as a reference. Cetrimide (CTAB) and Tetra Ethyl Ammonium Bromide (TEAB) were used as the surface directing agents. The spectra showing the progress of the reactions in IPA solvent are shown in the Fig. 1. The spectra of each freshly prepared solution before irradiation is shown in the curve (a). These sols are faint greenish in color and the rest of the spectra after the initiation till the termination of the irradiation are shown as curves (b – d). At the termination of the reaction the color of the sols were golden yellow. The change in the color of the sols indicates the formation of nanoparticles.

In the curves (a) of the Fig. 1 one can see the presence of a distinct peak in the range of 387 nm to 400 nm and a shoulder at 662 nm to 682 nm corresponding to the characteristic absorption of Ni^{2+}ions.

Sample synthesized without surfactant shows a peak at ~ 382 nm and a shoulder at ~ 583 nm in the Fig. 1 (A, curves b – d). The intensities of the peak and the shoulder formed during synthesis increase, at the termination of the reaction marked by the curve (d) and the absorption maxima shifts to the wavelength ~ 391 nm indicative of the formation of the intra -3d transition of Ni^{2+} ions in the cubic structure of NiO [22] and shoulder seen at ~ 587 nm may be attributed to the formation of the Ni_2O_3.

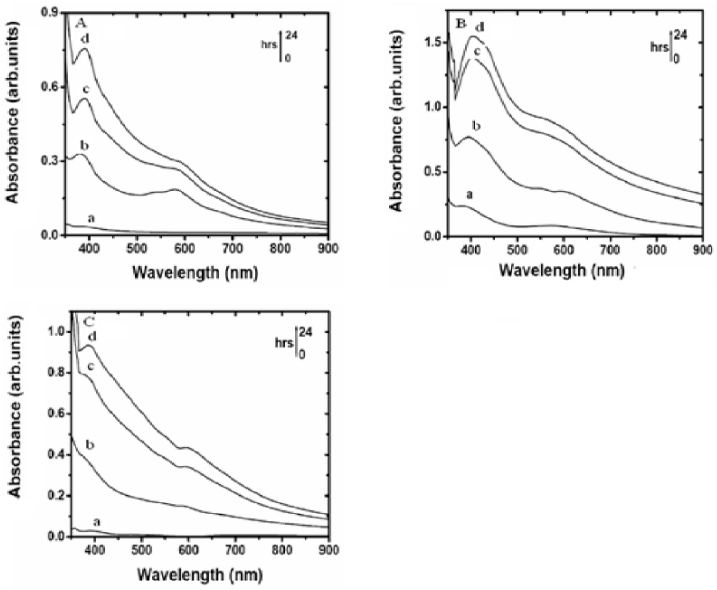

Fig. 1. UV-visible spectra of nickel oxide nanosols prepared by using 100% IPA with (A) No surfactant, (B) CTAB, (C) TEAB and the time of irradiation (a) 0 h, (b) 6 h, (c) 18 h and (d) 24 h.

Sols prepared with CTAB as surfactant shows a peak at ~ 396 nm and a shoulder at ~ 585 nm which appears to shift with an increment in irradiation time to ~ 385 nm and ~ 583 nm together with an increase in absorbance as shown in Fig. 1 (B, curves b – d). The peak and the shoulder can be attributed to the formation of the Ni^{2+} and Ni^{3+} ions respectively directing the formation of the oxides. It is known that the shift in the peak is due to the change in the size of the particles.

Absorption spectra of the sample synthesized using TEAB as surfactant are given in Fig. 1 (C, curves b – d). During initial stages the formation of a shoulder like pattern at ~ 590 nm can be observed, at higher time intervals of irradiation the peak is observed at ~ 383 nm indicative of the formation of NiO [22] and a shoulder may be assigned to Ni_2O_3.

The similarity indicates that the irradiated test solutions contain Ni_2O_3 particles and that the colloidal particle density increases with irradiation time. The good agreement between the reference spectrum and the test solution spectra also indicates that Ni^{3+} is the only colored species present.

Further, experiments were also carried out by using IPA-water solvent mixtures. The percentage of IPA was varied from 100% to 20%. Fig. 2 shows the UV-visible spectra of the synthesized samples.

The spectra of the samples synthesized in the absence of surfactant, Fig. 2(A), show a peak at λ_{max} of ~ 391 nm that shifts to ~ 457 nm with the increase in percentage of water in the solvent. Similarly, a shoulder at ~ 587 nm is also observed to shift to ~ 708 nm.

Fig. 2 (B) depicts the spectra of samples synthesized in the presence of CTAB which also shows shift in the peaks as for the above sample.

In case of TEAB as given in the Fig. 2 (C), the peak is observed in the range of 383 nm to 440 nm and a shoulder at 591 nm to 778 nm. The peak in the above samples can be attributed to the formation of octa-coordinated complex of NiO [23] and the shoulder for Ni_2O_3 with the polaron-π^* transitions of aniline oligomers [24].

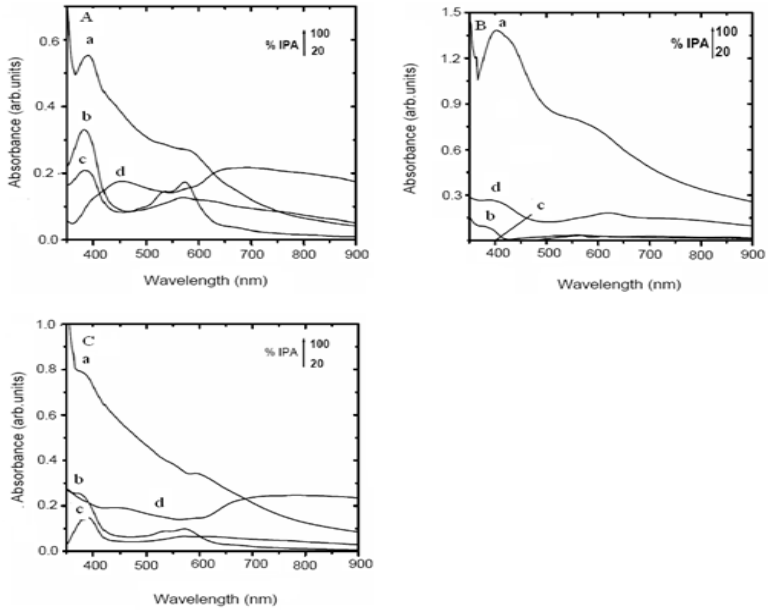

Fig. 2. UV-visible spectra exhibiting the effect of IPA-water combination on the nickel oxide nanosols synthesized by using (a) 100% IPA, (b) 80% IPA, (c) 50% IPA and (d) 20% IPA with (A) No surfactant, (B) CTAB and (C) TEAB.

Further, a sharp decrease in absorbance with increasing fraction of water in IPA is due to the lower yield of the products formed in water based solutions. Sharper peaks observed in the spectra in the presence of surfactants can be attributed to narrower size distribution of the product particles.

Table 1 presents the λ_{max} values of the samples synthesized with and without surfactant.

Table 1. λ_{max} observed in the UV-vis spectra of nickel oxide samples in (a) 100% IPA, (b) 80% IPA, (c) 50% IPA and (d) 20% IPA with (A) No surfactant, (B) CTAB and (C) TEAB.

Sample	λ_{max} (nm)		
	(A)	(B)	(C)
(a)	391	395	383
(b)	384	384	378
(c)	383	397	389
(d)	457	387	440

2) Fourier transform infrared spectroscopy

The functional groups were identified by FT-IR spectroscopy. Fig. 3 depicts the FT-IR spectra of the samples (without surfactant, with CTAB and TEAB) synthesized in IPA (100%) and 20% IPA. The spectra using 100% IPA is labeled as (a) and 20% IPA as (b).

From figure, one can note a peak ~ 412 cm^{-1} in case of samples synthesized in IPA (100%) corresponding to Ni-O stretching band of nickel oxide [25].

At the other extreme, that is 20% IPA the band observed at ~ 420 cm^{-1} also represents the formation of the oxide [25].

Peak at ~ 3200 cm^{-1} is assigned to the presence of water molecules present on surface [26]. Apart from these two peaks, the remaining bands observed in the inset of the figure as a full spectral region from 4000 cm^{-1} to 350 cm^{-1} are characteristic of the aniline oligomers and polymer exhibiting absorption peaks corresponding to the N-H stretching band in the range of 3200 cm^{-1} - 3050 cm^{-1}, the quinoid and benzenoid stretching seen at ~ 1570 cm^{-1} and ~ 1500 cm^{-1} respectively. All these peaks resemble with the standard polyaniline spectra [27].

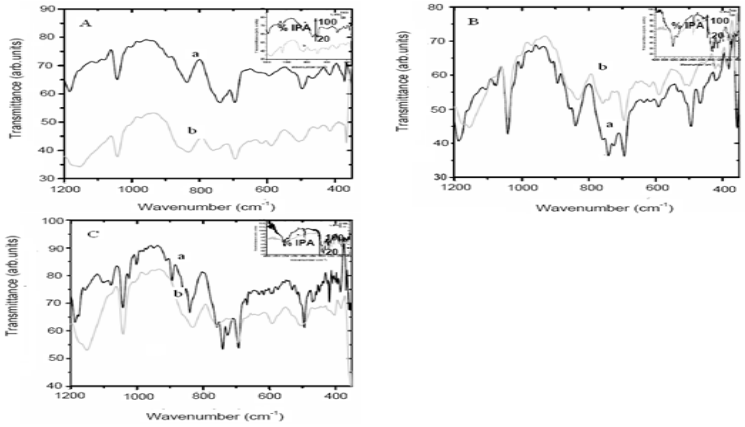

Fig. 3. FT-IR spectra of nickel oxide samples prepared by using in (a) 100% IPA and (b) 20% IPA with (A) No surfactant, (B) CTAB and (C) TEAB (inset 4000-350 cm^{-1}).

3) X-ray diffraction measurements

Fig. 4 show the X-ray diffractograms of samples prepared in IPA as solvent with and without surfactants along with their corresponding hkl values. The peaks observed at 2θ values of ~ 32.0° (002), ~ 39.3° (102), ~ 51.8° (112) and ~ 56.9° (202) depict the formation of Ni_2O_3 phase while peaks at ~ 37.4° (101), ~ 43.6° (012) and ~ 62.9° (104) represent the NiO phase of nickel oxide nanoparticles [28]. The peaks are indexed as Ni_2O_3 and NiO phases as per the ASTM standards 14-0481 and 44-1159 respectively.

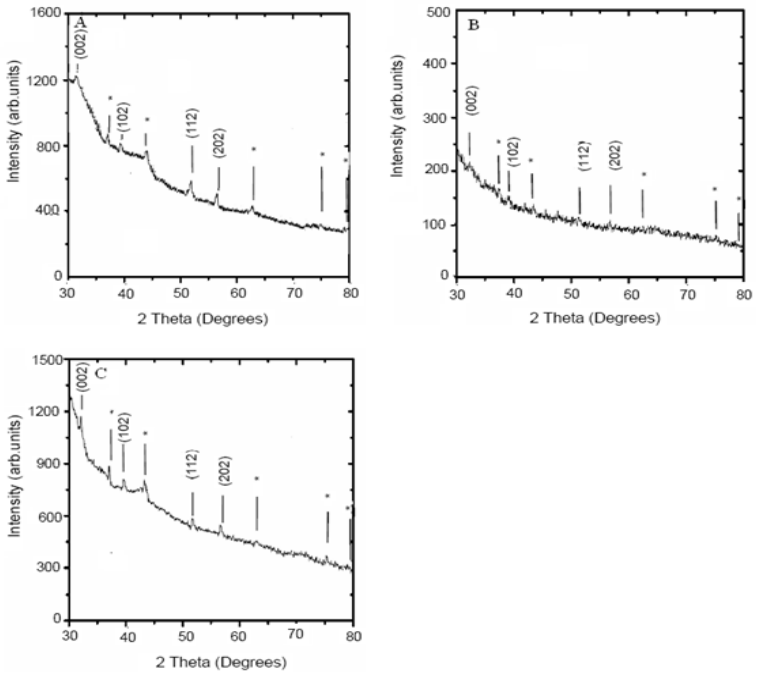

Fig. 4. X-ray diffractograms of nickel oxide samples synthesized in (a) 100% IPA and (b) 20% IPA with (A) No surfactant, (B) CTAB and (C) TEAB. (*) denote NiO phase and the remaining peaks are all of Ni_2O_3.

In the figure, the NiO phase is labeled by (*). The 100% intensity peaks in all diffractograms match with the Ni_2O_3 as the major phase. The comparative data sheet of these samples prepared is displayed in Table 2.

X-ray diffractograms showed very poor reflections for samples prepared in IPA-water mixture (1:4). Therefore, the data has not been included in the text.

Table 2 X-ray diffraction data showing 2θ and hkl values of nickel oxide samples synthesized in 100% IPA with (A) No surfactant (B) CTAB and (C) TEAB.

Sample containing 100% IPA	Ni_2O_3 phase		NiO phase	
	2 Theta	(hkl)	2 Theta	(hkl)
[A]	31.6°	(002)	37.3°	(101)
	39.0°	(102)	43.7°	(012)
	52.1°	(112)	63.0°	(104)
	56.7°	(202)		
[B]	32.0°	(002)	37.4°	(101)
	39.1°	(102)	43.6°	(012)
	51.8°	(112)	62.9°	(104)
	57.0°	(202)		
[C]	32.3°	(002)	37.4°	(101)
	39.5°	(102)	43.6°	(012)
	51.8°	(112)	63.0°	(104)
	57.1°	(202)		

4) Proposed reaction mechanism

Based on the experimental evidence, visual observations and the results obtained, general reaction mechanism proposed is as follows.

The alcohol undergoes radiolysis giving solvated electrons, hydroxide, isopropyl and acetonyl radicals along with other radiolysis products [29]

$ROH \rightsquigarrow e^-_{sol}, H_{sol}, OH^-, ROH_2^+, RCOH$ etc. 4.1

The species formed are the hydrated electrons, e^-_{aq}, hydroxyl radicals, $OH^\bullet$, and small traces of hydrogen atoms. These hydroxyl radicals and the hydrated electrons are the main reacting species in the irradiated solution. Similar kind of radiolytic reactions occur in all alcoholic solutions. The e^-_{sol} produced would be available for Ni^{2+} ions to reduce to Ni^+ present in the reaction mixture.

$Ni^{2+} + e^-_{sol} \rightarrow Ni^+$ 4.2

However, the Ni^+ ions are highly unstable and lead to the formation of oxides. The color of the solution exhibits a transition from a turbid green to golden yellow color.

$Ni^+ + Ni^+ \rightarrow Ni^0 + Ni^{2+} \rightarrow NiO + O_2 \rightarrow Ni_2O_3$ 4.3

Scheme 1 Proposed Reaction mechanism for the formation of nanosized Ni_2O_3.

5) Transmission electron microscopy

Fig. 5 shows the transmission electron micrographs of the samples prepared in IPA along with their corresponding selective area electron diffraction patterns. The respective particle size distribution is also displayed in the figure.

Fig. 5 (A, D and G) shows the microscopic images of the samples synthesized in the absence of surfactant, with CTAB and TEAB respectively. Spherical morphology can be observed in the sample without surfactant (Fig. 5, A). The particles appear to be agglomerated with an average particle size of ~ 50 nm.

Similarly, the sample with CTAB as surfactant (Fig. 5, D) appears spherical and is agglomerated forming clusters. The size of particles is larger in comparison with the average size of ~ 160 nm.

The samples prepared with TEAB as surfactant (Fig. 5, G) shows the formation of irregular shaped particles. They also appear to be agglomerated forming a garland like structure. The agglomeration observed in the particles is due to the presence of the magnetic forces present between them. The average size of the particles is ~ 200 nm in diameter.

The spherical or nearly spherical shaped morphology as seen in the nanoparticles in the case of the samples could be attributed to the fact that these materials were found out to be dynamic in nature and the particle morphology was kinetically controlled [30].

The respective SAED profiles are displayed in the Fig. 5 (B, E and H). These profiles were initially calibrated by using ‘d’ spacing on a single crystalline Au thin film and then the measurements for respective samples were carried out. Some broad as well as diffused rings are observed in all the synthesized samples. In the TEAB containing sample, some spots are noted along with the ring like patterns indicating the polycrystalline nature of the product.

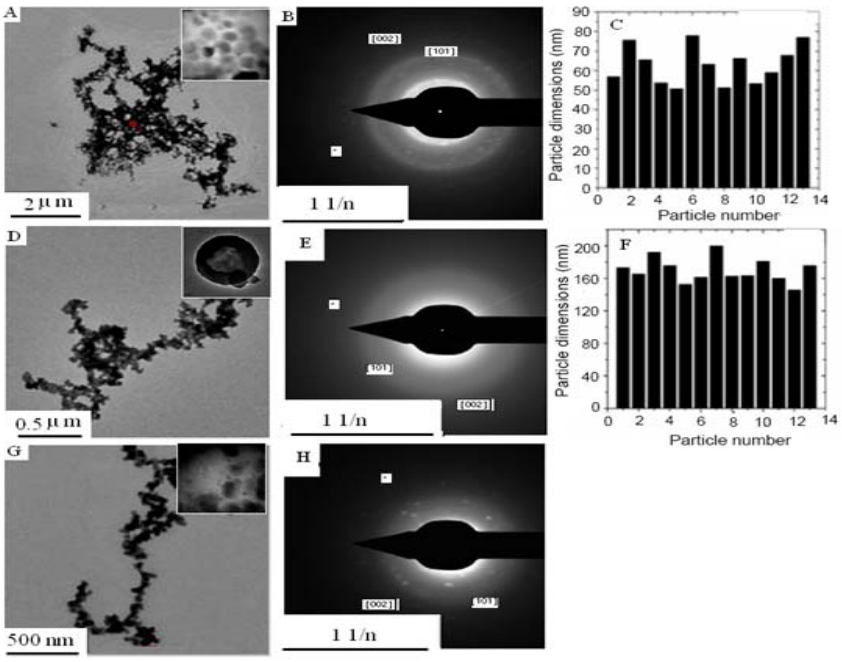

Fig. 5. TEMs of nickel oxide nanosols (100% IPA) with SAED patterns and particle size distribution (A) No surfactant, (D) CTAB and (G) TEAB, respective SAED patterns in (B), (E) and (H) and particle size distribution with (C) No surfactant and (F) CTAB.

These materials exhibit crystalline nature with the lattice constants of the rings present at ~ 0.35 nm, ~ 0.28 nm and ~ 0.25 nm. These values were indexed as per the standards available for identification as 14-0481 and 44-1159 assigned for the Ni_2O_3 and NiO phases respectively. The rings at ~ 0.35 nm and ~ 0.28 nm can be assigned to the formation of the Ni_2O_3 and ~ 0.25 nm can be allocated to the NiO phase. These 'd' values obtained from the SAED values are in close resemblance with the XRD results obtained, supporting the formation of the oxides.

The particle size distribution of all these samples is also presented in Fig. 5 The sample prepared in the absence of surfactant (Fig. 5, C) shows relatively narrow size distribution between 30 nm and 50 nm compared to those prepared in CTAB (Fig. 5, F) showing a broad distribution in size varying between 160 nm to 195 nm. Due to the irregular shape of the particles synthesized in TEAB, the size distribution could not be evaluated.

The elemental composition for determining the stoichiometric ratios and confirmation of the phase was carried out by using energy dispersive spectroscopy and high resolution transmission electron microscopy respectively.

The elemental compositions of individual elements, nickel and oxygen in all samples are depicted in Fig. 6 (A, D and G) together with matching fringe width computed by using Gatan imaging software as shown in Fig. 6 (B, C, E, F, H and I).

The presence of copper, oxygen, carbon and nickel can be seen in all the samples. Elemental copper comes from the copper grid used as sample holder and carbon in part from film on the surface of the copper grid and partially from the polymer carbonization [31,32]. The elemental ratio of nickel to oxygen is 1:1 which indicates the formation of the nickel oxide. These experimentally calculated proportions are in accordance with the theoretically obtained values. A comparative data sheet evaluated from the EDAX spectra for the elemental composition of nickel and oxygen is given in the Table 4.3.

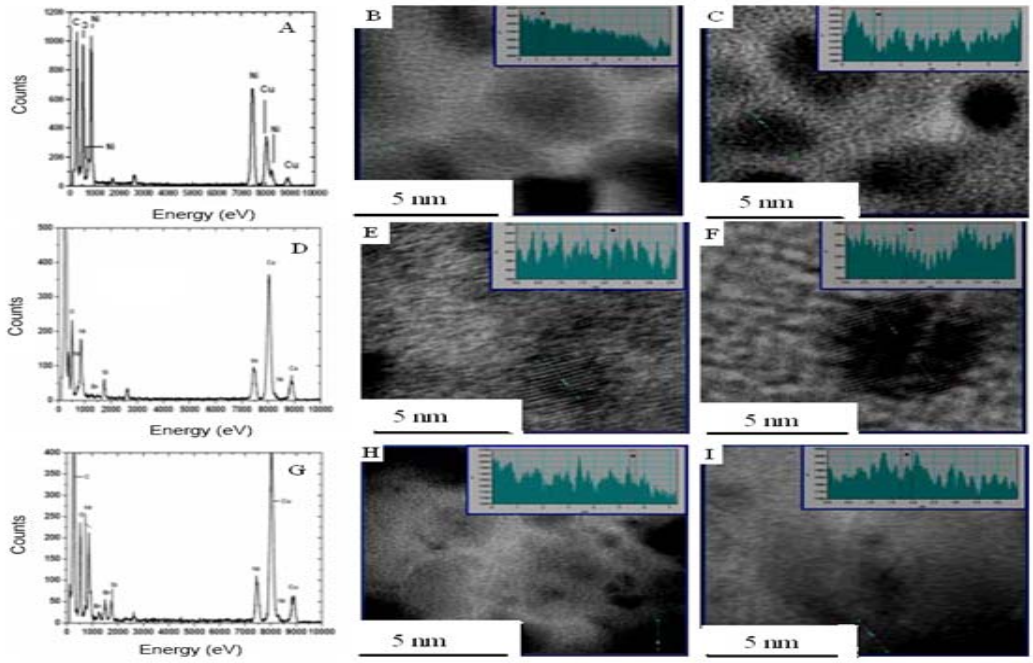

Fig. 6. EDAX of nickel oxide nanosols prepared in 100% IPA as solvent (A) No surfactant (D) CTAB and (G) TEAB with their HRTEM images in (B), (C), (E), (F), (H) and (I) respectively. (inset depicting the fringe width of the samples).

From HRTEM micrographs, one can observe the formation of the spheres confirming the morphology as seen in the TEM images. The inset of these HRTEM images clearly shows the lattice planes with a periodicity of 0.022 nm. The fringe widths acquired are ~ 0.23 nm and ~ 0.25 nm. The 'd' values obtained at ~ 0.23 nm can be assigned to Ni_2O_3 and ~ 0.25 nm for the NiO phase as per JCPDS card no. 14-0481 and 44-1159 respectively.

The results obtained from these 'd' values are in accordance with the XRD patterns and the SAED patterns confirming the formation of Ni_2O_3 as the major phase of nickel oxide.

At the other extreme, the TEMs, the diffraction patterns and the particle size distributions of the samples prepared in 20% IPA are presented in the Fig. 7. From the TEMs, Fig. 7 (A, D and G) one can observe partially spherical shape of the particles. The sample without surfactant exhibits individual particles with separate grain boundaries while in the presence of surfactant strong agglomeration is observed. The average particle size in the first two samples is ~ 75 nm (Fig. 7, A and D) while the latter one (Fig. 7, G) shows an average size of ~ 200 nm.

The corresponding labeled diffraction patterns are shown in Fig. 7 (B, E and H). Broad diffused rings can be observed in the diffraction patterns together with spots indicating the polycrystalline nature of the samples. The planes of the rings are marked as per the ASTM standards 14-0481 and 44-1159 corresponding to the Ni_2O_3 and the NiO phases respectively. 'd' spacings observed for these rings are found to be ~ 0.33 nm, ~ 0.28 nm and ~ 0.25 nm which after indexing were found out to be ~ 0.33 nm and ~ 0.28 nm assigned to Ni_2O_3 and ~ 0.25 nm to NiO phases respectively. In all these figures, the NiO phase is labeled by (*). These values match well with that of the standards along with 'd' values reported from the XRD patterns thus establishing the formation of the oxides.

It is observed that the size of the particles is in the range of 50 nm - 80 nm in samples without surfactant (Fig. 7, C), while the sample with CTAB (Fig. 7, F) shows a broad size distribution from 60 nm to 110 nm. In the case of TEAB samples the particle size distribution could not be found out as these particles showed strong agglomeration.

Data obtained from EDAX for elemental compositions is given in Table 3., and the phase confirmation micrographs are presented in Fig. 8. The elemental composition shows the presence of nickel, oxygen, carbon and copper. Copper is from copper grid and carbon is in part from carbon film on the surface of the grid and partially from the polymer carbonization [31,32]. The elemental compositions of these samples show the atomic percentages of nickel and oxygen as 35% and 45% respectively corresponding to the formation of the nickel oxide. The compositional data obtained from the EDAX spectra supports the theoretically calculated values indicating a good compositional homogeneity across the nanoparticles.

Table 3. Elemental composition of nickel oxide nanosols prepared in 100% IPA in (A) without surfactant, (C) CTAB and (E) TEAB and 20% IPA with (B) without surfactant, (D) CTAB and (F) TEAB.

Elements	Percentage					
	(A)	(B)	(C)	(D)	(E)	(F)
Ni	47	42	44	35	36	34
O	43	33	44	45	44	46

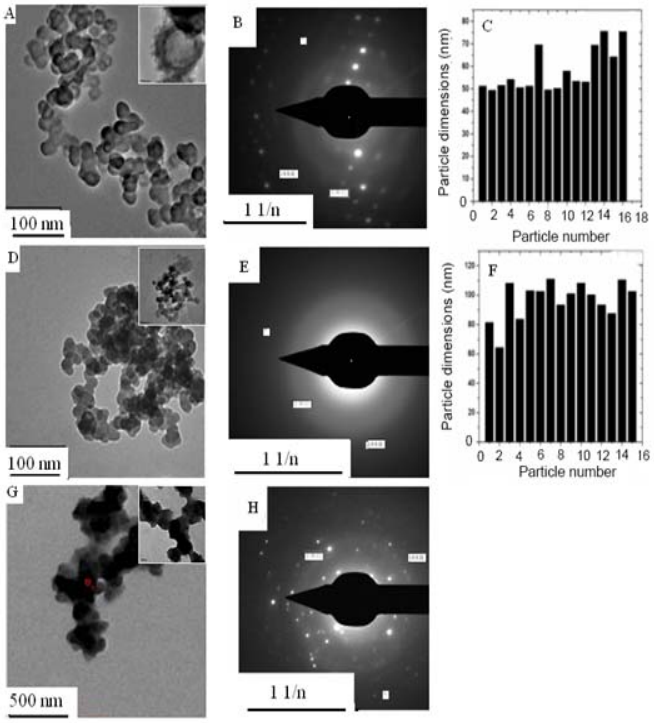

Fig. 7. TEMs of nickel oxide nanosols prepared in 20% IPA as solvent (A) No surfactant, (D) CTAB and (G) TEAB with SAED patterns in (B), (E) and (H) respectively and particle size distribution in (C) with No surfactant and (F) CTAB.

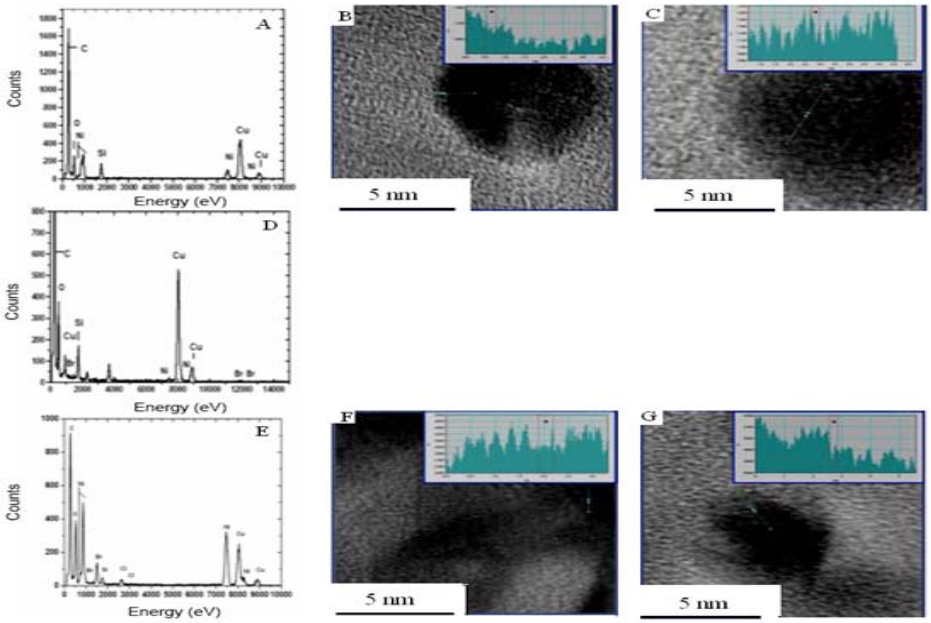

Fig. 8. EDAX of nickel oxide nanosols prepared in 20% IPA as solvent (A) No surfactant, (D) CTAB and (E) TEAB and HRTEM images with (B), (C) No surfactant and (F) and (G) with TEAB with inset depicting the fringe width of the samples.

The inter planar distances 'd' between the two lattice fringes were found out with the periodicity of lattice planes of 0.022 nm and are then matched with their respective standards to confirm the oxide formation.

'd' spacings as observed in Fig. 8 (B, C, F and G) are found to be ~ 0.30 nm and ~ 0.26 nm. The ~ 0.30 nm spacing can be assigned to Ni_2O_3 and ~ 0.26 nm to NiO phase. These values are in accordance with the ASTM standards corresponding to nickel oxide. The regular behavior of the lattice fringes inside the cluster suggests that most clusters have good crystalline structure with no defects. The overlapping of clusters in some areas of the image is due to the TEM sample preparation technique. The results are in close agreement with 'd' values obtained from the selective area electron diffraction patterns and the X-ray diffraction measurements establishing the formation of Ni_2O_3 formed as the major phase of the nickel oxide.

6) X-ray photoelectron spectroscopy

XPS analysis of the samples was carried out within an accuracy of 0.1 eV. Fig. 9 shows the plot for the XPS spectra of the samples synthesized using IPA (100%) as solvent. In all the spectra 'a' is labeled for the general scan while 'b' and 'c' represent the deconvoluted

oxygen and nickel spectra respectively. The values identified for particular species present are also marked in the figures along with the data given in Table 4.

As per the standard values provided by the NIST and reported values, the Ni2p spectra could be deconvoluted into five peaks with different binding energies. The reported values by NIST are viz. peaks corresponding to the binding energy values ~ 853.7 eV, ~ 855.6 eV, and ~ 861.0 eV are attributed to the $Ni2p_{3/2}$ peaks and peaks at binding energy values of ~ 872.4 eV and ~ 879.0 eV are assigned to $Ni2p_{1/2}$.

In Fig. 9(A) for the sample synthesized without surfactant, the spectrum shows the presence of two peaks present at the binding energy values of ~ 855.91 eV and ~ 873.97 eV. A peak seen at ~ 855.91 eV is in accordance with the standard data available for the Ni^{3+} oxidation state with the spin values of $Ni2p_{3/2}$ [33]. The binding characteristic of trivalent nickel oxide indicates the existence of Ni_2O_3 on the surface of the NiO which has the value as ~ 873.97 eV [34]. Along with the main peaks satellite peaks are noticed in the spectra. Satellite peaks position observed are at 861.59 eV and 880.76 eV which are indicative of the formation of Ni_2O_3 and NiO phases respectively

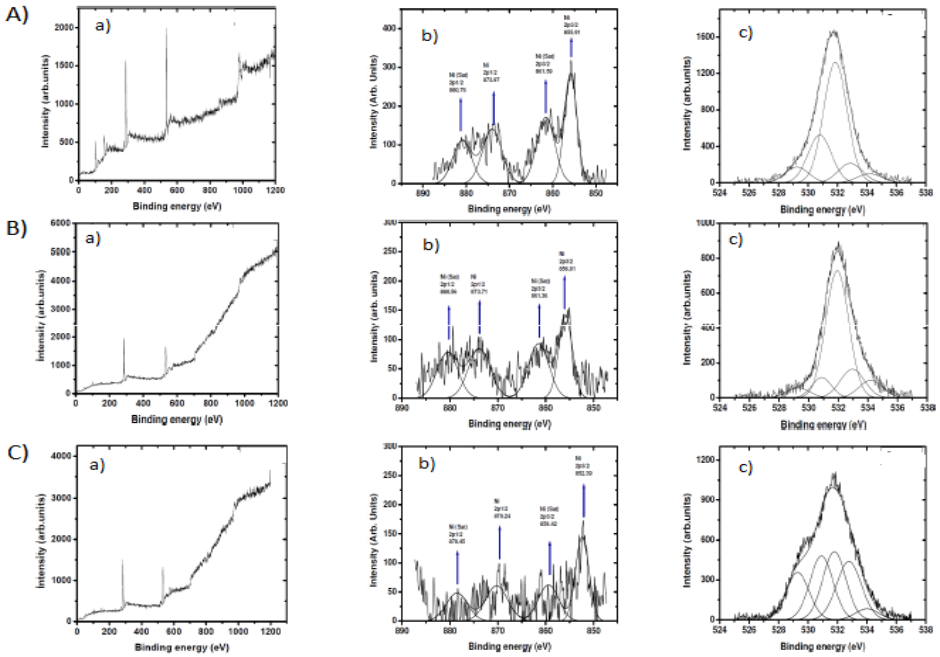

Fig. 9 XPS of nickel oxide nanosols prepared in 100% IPA as solvent (A) without surfactant, (B) CTAB and (C) TEAB (a) general, (b) oxygen and (c) nickel scans.

Similar spectrum is observed for samples synthesized with CTAB (Fig. 9, B). The peaks corresponding to Ni_2O_3 [33] and NiO [34] are observed at similar positions as before. Peaks are seen at 856.01 eV and 873.71 eV. In addition to this, one can also note the

appearance of the satellite peaks at ~ 861.36 eV and ~ 880.56 eV which are assigned to the oxide phase of the samples which match with the respective oxides of Ni_2O_3 and NiO.

Sample prepared in TEAB exhibit peaks at ~ 852.39 eV and ~ 870.24 eV (Fig. 9, C). The corresponding spin orbital coupling (peaks) of these oxides are $Ni2p_{3/2}$ (852.39 eV) and $Ni2p_{1/2}$ (870.24 eV). These peaks are assigned to the respective oxides as per the standards available. Along with the shift in the main peaks, the shift in satellite peaks is also distinctly seen. The satellite peaks are seen at ~ 859.42 eV and ~ 878.45 eV. These are also indicative of spin orbital coupling of the oxides. The shift in the main and the satellite peaks may be due to the decrease in the particle size of the samples and also due to strong agglomeration as seen as particles are magnetic in nature and irregular shape of the particles.

Further, from the oxygen spectra as seen in the figure and the corresponding data given in the Table 5, the peak present at ~ 531.70 eV with the maximum intensity confirms the presence of Ni^{3+}, seen as the major oxidation state and Ni_2O_3 as the oxide phase.

During the synthesis, $Ni(OH)_2$, NiO and Ni_2O_3 are produced due to the interaction of H_2O with Ni. As there is too little water in the reaction mixture to form any hydrogen containing species, we obtain a mixture of Ni (II), and Ni (III) chemical oxidation states in these samples establishing the formation of Ni_2O_3 as the major phase.

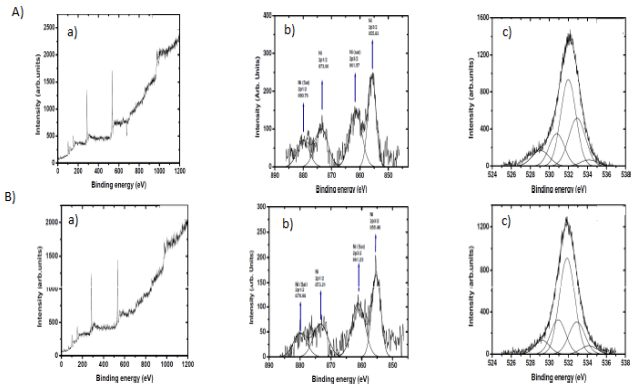

Fig. 10. XPS of nickel oxide nanosols prepared by using 20% IPA as solvent (A) without surfactant, (B) TEAB (a) general, b) oxygen and (c) nickel scans.

XPS of the samples prepared by using IPA water combination (1: 4) are shown in the Fig. 10. The curves 'a', 'b' and 'c' seen in the spectra are marked for general, oxygen and nickel scans in the same order.

NIST standards indicate presence of the peaks for Ni^{3+} present at ~ 853.7 eV, ~ 855.6 eV and ~ 861.0 eV with the spin orbital coupling as $Ni2p_{3/2}$ and peaks with binding energy values ~ 872.4 eV and ~ 879.0 eV are attributable to Ni^{2+} with splitting seen as $Ni2p_{1/2}$.

Fig. 10(A) shows the presence of two distinct peaks at binding energy values of ~ 855.83 eV (Ni^{3+}) and ~ 873.60 eV (Ni^{2+}) for the samples without surfactant. The spin orbital couplings observed for the corresponding oxides are $Ni2p_{3/2}$ and $Ni2p_{1/2}$ that can be assigned to Ni_2O_3 [26] and NiO [34] states respectively. The satellite peaks observed at ~ 861.57 eV and ~ 880.76 eV correspond to the formation of the oxides, data is given in Table 4.

Table 4. X-ray photoelectron spectroscopy data obtained for nickel oxide synthesized in 100% IPA (A) No surfactant, (B) CTAB and (C) TEAB, and 20% IPA in (D) No surfactant and (E) TEAB.

Samples	Binding Energy (eV)			
	Ni_2O_3 ($2p_{3/2}$[a])		NiO ($2p_{1/2}$[a])	
	Peak	Satellite	Peak	Satellite
(A)	855.91	861.59	873.97	880.76
(B)	856.01	861.36	873.71	880.56
(C)	852.39	859.42	870.24	878.45
(D)	855.93	861.57	873.60	880.76
(E)	855.48	861.23	873.21	879.98

[a]Spectral line of Ni_2O_3 and NiO peaks.

Similar observations are noted for samples synthesized with CTAB (Fig. 10,B). Table 4 presents the exact binding energy values for the respective species. The peaks are obtained at ~ 855.48 eV and ~ 873.21 eV which corresponds to the formation of Ni_2O_3 and NiO as the respective oxides. At a similar position as the spectra seen in the samples synthesized without surfactant reported previously one can see that the satellite peaks. These satellite peaks are seen at ~ 861.23 eV and ~ 879.98.eV can be reported for the formation of Ni^{3+} and Ni^{2+} oxidation phase respectively.

O (1s) spectra is also presented in the Fig.10. The binding energy values at ~ 531.92 eV and ~ 529.21 eV are assigned to the presence of Ni^{3+} and Ni^{2+} oxidation states of the oxide nanoparticles respectively. The data is given in Table 5.

Table5. XPS data for nickel oxide sample synthesized by using 100% IPA (A) with No surfactant, (B) CTAB and (C) TEAB and 20% IPA with (D) No surfactant and (E) TEAB.

Samples	Binding Energy (eV)	
	Ni_2O_3 O(1S) [a]	NiO O(1S)[a]
	Peak	Peak
(A)	532.05	529.19
(B)	532.95	529.21
(C)	532.79	529.29
(D)	531.90	529.02
(E)	532.89	529.18

[a]Spectral line of Ni_2O_3 and NiO peaks.

CONCLUSIONS

Nickel oxide nanoparticles are obtained by using steady state gamma radiolysis. Different surfactants are used for the synthesis. Nearly spherical or spherical particles of smaller dimensions are obtained. XPS analysis confirms the formation of Ni_2O_3 as the major phase formed during the synthesis of the nanoparticles.

ACKNOWLEDGEMENTS

The authors thank IIT, Powaii for TEM and XRD analysis, TIFR Mumbai for XRD analysis. . Authors would like to acknowledge DST Unit for Nanoscience, University of Pune, Pune. KNK would like to thank CNQS, University of Pune, Pune as well as UGC, for partial financial support and Prof B.S.M. Rao for fruitful discussions.

REFERENCES

1. Bin, Z., Xiao, K. K., Jian, H. B., Chun, L. W., Lin, D., Yu, W. C. and Hui, L. C. (2009). Synthesis of flower-like NiO and effects of morphology on its catalytic properties. J Phys Chem C, 113: 14440-14447.
2. Capek, I. (2004). Preparation of metal nanoparticles in water-in-oil (w/o) microemulsions. Adv Colloid Interface Sci, 110: 49-74.
3. Ceylan, A., Rumaiz, A. K. and Shah, S. I. (2007). Inert gas condensation of evaporated Ni and laser ablated CoO. J Appl Phys, 101: 094302.
4. Chen, D. H, and Hsieh, C. H. (2002). Synthesis of nickel nanoparticles in aqueous cationic surfactant solutions. J Mater Chem, 12: 2412-2415.
5. Chih, J. C., Hsin, Y. L., Chee, C. L., Jiun, S. W. and Ray, K .C. (2009). Preparation of monodisperse iron oxide nanoparticles via the synthesis and decomposition of iron fatty acid complexes. Nanoscale Res Lett, 4: 1343–1350.
6. Curri, M. L., Agostiano, A. and Mavelli, F. (2002). Reverse micellar systems: self organised assembly as effective route for the synthesis of colloidal semiconductor nanocrystals. Mater Sci Eng C, 22: 423-426.

7. Daou, T. J., Pourroy, G., Bgin, C. S., Grenche, J. M., Ulhaq, B. C., Legar, P., Bernhardt, P., Leuvrey, C. and Rogez, G. (2006). Hydrothermal synthesis of monodisperse magnetite nanoparticles. Chem Mater, 18: 4399-4404.
8. Deraz, N. M. (2012). Formation and magnetic properties of metallic nickel nano-particles. Int J Electrochem Sci, 7: 4608-4616.
9. Feng, S. X. and Lian, G. (2008). Facile synthesis of polycrystalline NiO nanorods assisted by microwave heating. J Am Ceram Soc, 91**:** 3465-3468.
10. Han, D. Y., Yang, H. Y, Shen, C. B., Zhou , X. and Wang, F. H. (2004). Synthesis and size control of NiO nanoparticles by water-in-oil microemulsion. Powder Technol, 147: 113-116.
11. Hernandez, T. J. and Mendoza, A. G. (2005). Optical properties of sol–gel SiO_2 films containing nickel. Thin Solid Films, 472: 130-135.
12. Hideyuki, Y. (2006). Protein-assisted nanoparticle synthesis. Colloid Surface A, 282-283: 464-470.
13. Hong, B., Shandong, L., Jiang, X., Du, Y. and Yang, C. (2003). Magnetic anisotropy in carbon encapsulated Co/CoO "lines" with large exchange bias. Phys Lett *A*, 307: 69-75.
14. Jianfen, L., Rong, Y., Bo, X., David, T. L., and Dong, H. L. (2008). Development of nano-NiO/Al_2O_3 catalyst to be used for tar removal in biomass gasification. Energy Fuel, 22**:** 16-23.
15. Khanahmadzadeh, S. and Barikan, F. (2014). Fabrication and magnetic properties of polyimide/nickel oxide nanocomposite. Int J Nano Dim Ens, 5: 365-370.
16. Klabunde, K. J. (2001). Nanoscale Materials in Chemistry. Wiley Interscience, New York pp 49.
17. Leevin, D. and Ying, J. Y. (1997). Oxidative dehydrogenation of propane by non-stoichiometric nickel molybdates. Stud Surf Sci Catal, 110: 367-373.
18. Lu, K. and Zhu, X. (2009). Nickel–boron nanolayer evolution on boron carbide particle surfaces during thermal treatment. Thin Solid Films, 517: 4479-4483.
19. Masoud, S. N. and Fatemeh, D. (2009). Synthesis of copper and copper(I) oxide nanoparticles by thermal decomposition of a new precursor. Mater Lett, 63: 441–443.
20. Miller, E.L. and Rocheleau, R. E. (1997). Electrochemical behavior of reactively sputtered iron-doped nickel oxide. J. Electrochem Soc, 144: 3072-3077.
21. Mohamed, B. Z., Ming, H., Rahul, R. S., Malay, P., Kimiko,nT., Victor, M., Seyong, C., Shi, X. D., Jung, H. K., Masataka, I., Shinsuke, I. and Yusuke, Y. (2015). Controlled synthesis of nanoporous nickel oxide with two-dimensional shapes through thermal decomposition of metal–cyanide hybrid coordination polymers. Chem Eur J, 21: 3605-3612.
22. Moncada, E., Quijada, R. and Retuert, J. (2007). Nanoparticles prepared by the sol-gel method and their use in the formation of nanocomposites with polypropylene. Nanotechnology, 18: 335606.
23. Narayan, R. V., Vinod, K. and Aruna, D. (2006). Tuning size and catalytic activity of nano- clusters of cobalt oxide. J Chem. Sci, 118**:** 179-184.
24. Richard, C. F. and Melissa, M. L. (1995). Particle structure control in nanoparticle synthesis from the vapor phase. Mat Sci Eng A, 204: 113-124.
25. Sasi, B. and Gopchandran, K. G. (2007). Nano structured mesoporous nickel oxide thin films. Nanotechnology, 18: 115613.
26. Selvan, S. T., Hayakawa, T., Nogami, M. and Moeller, M. (1999). Polypyrrole–palladium nanocomposite coating of micrometer-sized polymer particles toward a recyclable catalyst. J Phys Chem B, 103:7441-7448.
27. Seo, H. J. and Yun C. K. (2008). Nano-sized manganese oxide particles prepared by low-pressure spray pyrolysis using FEAG process. Mater Res Bull, 43: 590–600.
28. Spinks J. W. T. and Woods, R. J. (1990). An introduction to radiation chemistry, 3rd edn Wiley.
29. Tadafumi, A., Yukiya, H., Kiwamu, S. and Kunio, A. (2001). Hydrothermal synthesis of metal oxide nanoparticles at supercritical conditions. J Nanopart Res, 3: 227-235.
30. Tang, J., Jing, X., Wang, B. and Wang, F. (1988). Infrared spectra of soluble polyaniline. Synth Met, 24: 231-238.
31. Xiaofeng, C., Xingfang, H. and Jingwei, F. (1995). Nanostructured nickel oxide films and their electrochromic properties. Nanostructured Materials, 6: 309–312.
32. Yang, H. X., Dong, Q. F. and Hu, X. H. (1998). Preparation and characterization of $LiNiO_2$ synthesized from $Ni(OH)_2$ and $LiOH{\cdot}H_2O$. J. Power Sources, 79: 256-261.
33. Ying, W., Yiming, H., Tinghua, W., Tong, C., Weizheng, W. and Huilin, W. (2007). Influence of some parameters on the synthesis of nanosized NiO material by modified sol–gel method. Mater Lett, 61: 3174-3178.
34. Yoshio, M., Todorov, Y. and Yamato, K. (1998). Preparation of $LiyMnxNi_{1-x}O_2$ as a cathode for lithium-ion batteries. J Power Sources, 74: 46-53.